Numerical modeling of Fabric Reinforce Cementitious Matrix composites (FRCM) in tension

Elisa Bertolesi, Francesca Giulia Carozzi, Gabriele Milani *, Carlo Poggi

Department of Architecture, Built Environment and Construction Engineering (ABC), Politecnico di Milano, Piazza Leonardo da Vinci 32, 20133 Milano, Italy

Received 23 June 2014
Received in revised form 4 August 2014
Accepted 6 August 2014

1. Introduction

The utilization of FRP (Fiber-reinforced Polymers) strips as reinforcements for structural elements instead of conventional methods is nowadays rather diffused in the rehabilitation and seismic upgrading of masonry buildings. The advantages are: limited

* Corresponding author.
E-mail address: gabriele.milani@polimi.it (G. Milani).

invasiveness, speed of execution, and good performance at failure [1–11]. The FRP strengthening technique entails however several drawbacks, as for instance low vapor permeability, poor behavior at elevated temperatures, incompatibility of resins on several substrate materials, relative high cost of epoxy resins, and, last but not least, no possibility to make the intervention reversible [12].

The use of inorganic matrices is a valid alternative to these problems [11]. However, it is well known that cement based materials have low tensile strength and are not ideal to impregnate fibers and yarns. In the last two decades, two innovative types of reinforcements for cementitious matrices have been experimented and studied. They are: short fibers (FRC, Fiber Reinforced Concrete [13]) and continuous fibers in a fabric form (TRC, Textile Reinforced Concrete).

Fabric reinforced cementitious matrix (FRCM) composites, examined in this paper, are a particular type of TRC [14] where a dry-fiber fabric is applied to a structure by means of a cementitious mortar strengthened with short fibers randomly disposed. The mechanical properties of FRCMs strongly depend on the bond between the fibers and the matrix and may vary if the yarns of the fabrics are pre impregnated with resin [15,16].

When compared with FRP composites, FRCM composites exhibit several advantages, as a greater resistance to high temperatures and ultraviolet radiations as well as a better compatibility with the substrates [17,18]. Finally, the reversibility of the intervention is much higher.

The typical failure mode of a FRP strip is the debonding from the reinforced substrate.

Debonding is always associated to a brittle behavior [12,19,20] and several numerical and analytical models are now available for practitioners to evaluate the peak strength, the relevant slip, the optimal anchorage lengths, etc.

Some specialized national codes and recommendations are also available to design a rehabilitation intervention with FRPs. Such recommendations are the results of a comprehensive and long experimental round robin tests, numerical investigations and semi-analytical approaches.

On the contrary, for FRCM composites, despite their increasing and quick diffusion in practice, various aspects still need to be studied. Several research groups are independently carrying on programs aimed at (1) conceiving simple experimental set ups to be standardized and (2) proposing numerical models (usually based on non-linear FEs) capable of reasonably fitting experimental evidences and predicting the actual behavior of FRCM composites.

From an experimental standpoint, it is important to notice that recently a synergic collaboration among three European universities, permitted the publication of some preliminary experimental results [21] (carried on independently) regarding the performance of three reinforcement systems made out of steel, carbon and basalt textiles embedded in inorganic matrices under uniaxial tensile coupon testing and bond tests on brick and stone substrates. The final aim is to have an insight into the behavior of such strengthening material when subjected to standard condition, putting the bases for a sort of round robin test already applied successfully in the case of FRP strips [22].

From a numerical point of view the situation appears more fragmented. The research group of RWTH Aachen University seems the most active in this field and it was probably the first to propose advanced numerical tools (mainly based on FEs) [23–27] for TRC composites subjected to various loading condition, including stochastic modeling of imperfections (such as scatter of material properties) under monotonic and cyclic loads.

In this context, the present work examines in detail the strengthening with FRCM composites from a numerical point of view focusing on tensile behavior. The analyses are based on *ad-hoc* designed experimentation, and are oriented to provide a mechanical understanding of the experimental behavior, in view of the FRCM composites application to historical masonry substrates.

A wide experimental program is ongoing at the Politecnico di Milano on a series of FRCM coupons subjected to direct tensile tests, with the final aim of proposing simple characterization tests to be eventually standardized in newly conceived technical norms [7].

The typical stress–strain behavior observed, in agreement with existing experimental works available in the literature, is a tri-linear curve, with a first phase that increases linearly according to Young's modulus of the mortar, a second phase where the cracks in the mortar start to grow, and a last phase in which the mortar is fully cracked and the curve assumes the same slope of the stiffness of the fabric [28]. A quite wide experimental scatter of the axial force–displacement curves was found, especially in the second phase. This can be caused by many factors, the most important being probably the disposition of the yarns in a non-straight shape.

In order to have an insight into the reasons at the base of the relatively wide scatter observed, a comprehensive numerical investigation was conducted by means of a FE discretization of the coupons, where the yarns were modeled by means of elasto-fragile truss elements and the reinforced mortar with either elasto-fragile or elasto-ductile plane-strain elements. In order to numerically predict the experimentally observed scatter, different kinds of imperfections (geometric and mechanic) are considered in the model. It is worth noting that, whilst the idea is rather classic since other researchers attempted in the recent past to account for various sources of imperfections associated with the fabrication of plain weave textile composites [29,30], it is the first time that the procedure is systematically applied to FRCM coupons subjected to direct tensile tests.

In particular, three different sets of simulations were performed, labeled from 1 to 3. In Set 1, yarns geometry was assumed deviating from the straight configuration. As a matter of fact, it was quite difficult (or almost impossible) to measure the deviation of the yarns from the mid-plane in the specimens. A reasonable assumption was to adopt a sinusoidal shape that can be justified by the geometry of the fabric with regular crossings of the warp and weft yarns in the grids. The assumption was consistent also with the method of preparation of the specimens, which does not consider a preliminary pre-stressing of the yarns. The numerical investigation was conducted varying (a) the sinusoid wavelength, (b) the maximum deviation from the straight configuration and (c) the mechanical behavior of reinforced mortar (elasto-brittle or elasto-ductile).

In Set 2, the whole specimen was assumed with an initial deformation due to a global bending of the coupon. This was detected in some specimens before their introduction into the testing machine. The curvature was certainly due to the shrinkage of the cementitious matrix during curing. The presence of a geometrical imperfection can even be caused by the high slenderness of the specimens. Indeed, one of the general indications recommended to technicians is that particular care in the installation of the coupon inside the testing machine should be adopted. Three values of increasing curvature were investigated, which fully demonstrated that an initial deviation from the straight configuration may have a considerable effect on the overall force–displacement behavior in tension.

In Set 3, the specimen was supposed initially cracked in different positions, before being introduced in the testing machine and tested. Again, the formation of micro-cracks is very likely even only handling the coupons before and during their installation in the experimental machine. This is due to the reduced mortar cross section, the specimen slenderness and the relatively limited tensile strength of the mortar.

Another objective of the present work was to study and compare possible constitutive models for the cementitious matrix to simulate the experiments. Three different material models were used for the mortar in the FRCM specimens in tension. The first model is an elastic perfectly-plastic Mohr Coulomb material with limited ductility. The second and third are softening damaging material with low and higher fracture energy.

From an overall analysis of simulations results, it can be affirmed that numerical models are capable of satisfactory reproducing experimental evidences and provide useful hints to justify the relative large scatter of the data observed experimentally.

2. Experimental investigation

In this section, the results of a wide experimental program still ongoing at the Testing Laboratory for Materials and Structures of the Politecnico di Milano are summarized. Initially, the results of the mechanical characterization of the constituent materials are presented, whereas in the second part of the section the experimental behavior of FRCM systems under tension is discussed.

2.1. Mechanical properties of the components

Fabric reinforced cementitious matrix systems (FRCM) consist of two main elements, a cementitious mortar with a low dosage of dry polymers and a reinforcing fiber grid. The system studied in this work is composed by a cementitious mortar and a PBO (polyparaphenylene benzobisoxazole) fiber grid. The PBO fibers are organized in an unbalanced net made with 10 mm and 20 mm spaced rovings. The free space between the rovings is 5 mm and 15 mm in the two directions and the nominal equivalent thickness in the two fibers directions is 0.046 mm and 0.011 mm respectively, see Fig. 1.

Tensile tests on dry rovings taken in the warp and weft directions were performed according to EN ISO 10618 [3]. Even a strip of the grid including 4 yarns in the warp direction was tested. Further details may be found in [7]. The tests were carried out under displacement control with a testing speed of 0.5 mm/min. The average values of the experimental results are summarized in Table 1. The observed failure mode was in most of the cases limited to the outer filaments that are subjected to higher stresses compared with the inner filaments. For this reason the obtained ultimate stress is lower than the nominal value reported in the technical sheets.

Indirect tensile test (Brazilian test) were performed on the cementitious mortar according to EN 12390-6 [4] and the results are reported in Table 1.

2.2. Mechanical characterization of the FRCM systems

As shown in the literature [5–7], it is today accepted that the constitutive behavior of FRCM composites in tension could be idealized as tri-linear (Fig. 2). In the first phase the material is uncracked and the composite exhibits a linear behavior. The second phase starts with the first formation of a crack (point T_1 in Fig. 2). In this state there is a significant decrease of the stiffness and relatively thin cracks appear gradually when the tensile stress increases and spread over the full length of the specimen [7]. This causes several oscillations in the load–displacement (or stress–strain) curves and a consequent larger variability of E_2. The third phase (starting in T_2) is the crack-widening region, where only few new cracks appear while the existing cracks become wider up to the final failure when the tensile strength of the textile is reached. In this phase, the only resistant part in the composite is the fabric and, therefore, the stress–strain curve becomes almost linear and should ideally reproduce the elastic modulus of the dry fibers. Fig. 2 represents the typical stress–strain trilinear behavior of a FRCM subject to tensile test compared to a tensile test of a specimen made with dry fibers.

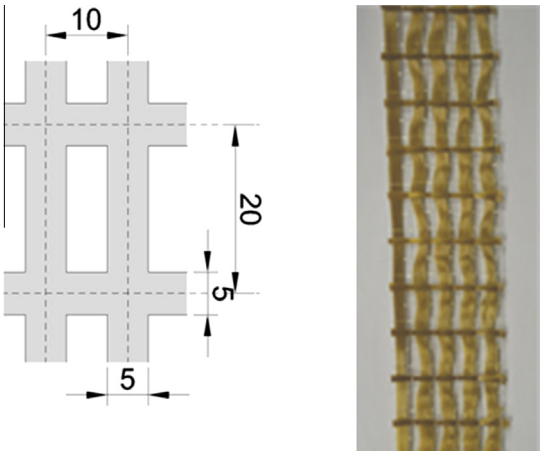

Fig. 1. PBO unbalanced net used in the present experimental tests.

Tensile coupons were made in a flat mold by applying a first layer of cementitious mortar (with a thickness of approximately 5 mm), one layer of PBO mesh and a second layer of cementitious mortar (5 mm). The coupons were cured for 28 days and had nominal size of $400 \times 40 \times 10$ mm (Fig. 3). As expected, a significant variability in the transversal section (both width and thickness) was observed with a maximum deviation from the nominal section equal to $+78/-137$ mm^2. This makes impossible to define a specific volumetric reinforcement ratio for each specimen. Therefore only one volumetric reinforcement ratio was adopted for the whole series making reference to the nominal mortar area (400 mm^2) and the resulting value was equal to 0.0046.

Tensile tests were carried out according to AC 434 guidelines but a different gripping mechanism was assumed as described in [7]. The test was executed under displacement control at 0.3 mm/min. This was increased to 0.5 mm/min after the end of the second phase. An extensometer with a gauge length of 100 mm was used to measure the strains in the central area of the specimens (Fig. 4).

A series of 11 tensile tests was examined to characterize the behavior of the FRCM coupons under tensile tests. In all tests, the stress–strain (or force–displacement) behavior was tri-linear, as shown in Fig. 5. The results present a rather large variability in particular in the loads corresponding to points T_1 and T_2 (Fig. 2). This may be caused by several factors: the irregularities of the cross section or warping of the specimens and irregular positions of the reinforcement in the thickness. The variability of moduli E_1, E_2 was mainly caused by the location of the first crack with respect to the extensometer that can appear outside the gauge length. Table 2 shows the main results: mean values, minimum, maximum and the coefficient of variation (StD/mean values). The elastic moduli of the three phases (E_1, E_2, E_3) reported in Table 2 were derived dividing the load by A_{fibers} (fiber cross section) because this is the only known geometric parameter that is not subject to possible changes during the manufacturing of the FRCM composite. On the contrary, mortar thickness and width show significant dispersions and are not a priori known. Only the last two columns in Table 2 are referred to the composite cross section, for comparison with mortar mechanical properties.

The average stress in the mortar (σ^*_{t1}) at the point T_1 (appearing of the first crack) is 3.65 MPa with a standard deviation (StD) of 1.10. This value can be compared with the maximum tensile strength of the mortar (4.75 MPa). The average slope of the third phase (215.8 GPa) is very similar to the elastic modulus of the dry textile (216 GPa).

3. Numerical models for test result interpretation

A series of simplified numerical models were used to interpret the experimental results. Particular attention was focused on two key features exhibited by the experimental evidences, namely the clear tri-linear behavior and the relatively large scatter of the load–displacements curves.

FRCM coupons were discretized into Finite Elements (FEs), using four-noded non-linear elements in plane-stress for mortar and two-noded truss elements to model the yarns. Bubble interpolation functions are used for mortar to eventually avoid shear locking phenomena in presence of bending (here possible thanks to the non-straight configuration of the yarns), in both the linear and non-linear range. A plane-stress assumption appears reasonable in this case, as a consequence of the free-stress conditions imposed on lateral faces, despite the width of the specimen is much higher (40 mm) than its thickness (10 mm). In this framework, the transversal area of the yarns is constituted by the overall area of the single yarns present in the coupon. Authors experienced engineering not relevant differences with a full 3D model, which however would require a much higher computational effort to be analyzed, especially in the non-linear range.

The following three different sets of numerical simulations are critically investigated, hereafter labeled as Set 1, Set 2 and Set 3 (see Figs. 6 and 7):

1. Set 1 is constituted by a family of numerical models where the yarn is supposed not-straight and exhibits a shape which follows a sinusoidal law of the type $y = a \sin\left(\frac{\pi x}{2l}\right)$, where a and l stand for the amplitude and wavelength of the yarn, respectively. Several different configurations are investigated in the

Table 1
Mechanical properties of PBO fibers and cementitious mortar.

Material	Tensile test	# Tests	Average failure stress (MPa)	C.o.V. (%)	Elastic modulus (GPa)	C.o.V. (%)
PBO	Single roving in the warp direction	6	3905	3.2	215.9	20.8
	Single roving in the weft direction	2	3430	–	276.6	–
	Grid strip of width 4 cm (4 Rovings)	4	3397	7.2	–	–
Mortar	Brazilian test	7	4.75	4.05	>6 (Data sheet)	–

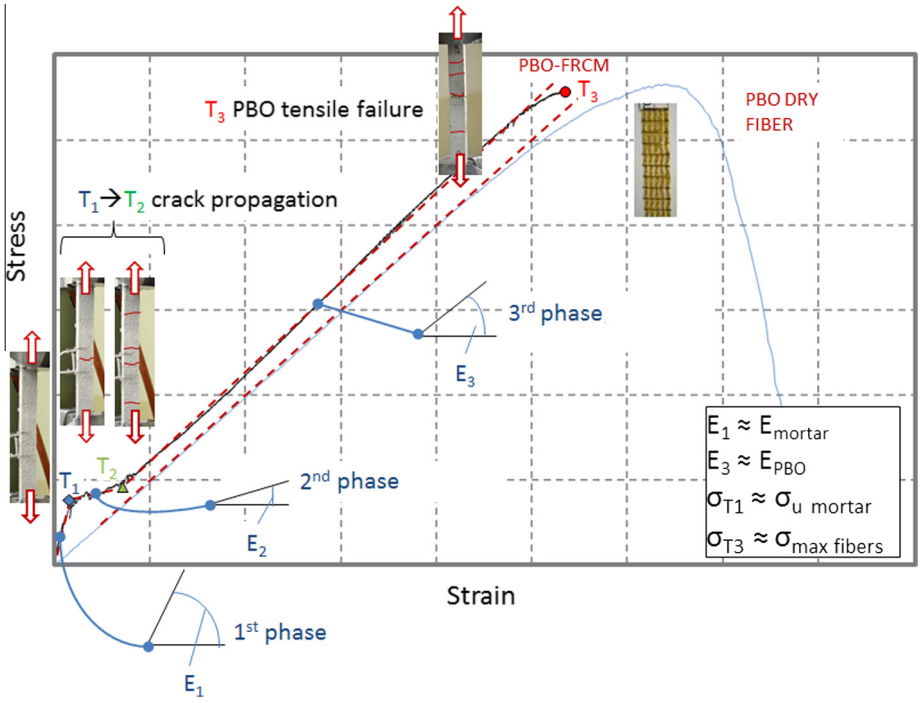

Fig. 2. Typical behavior of FRCM under tension.

numerical analyses, studying 4 amplitudes (equal to 0.5, 1, 1.5 and 2 mm) and 3 wavelengths (equal to 20, 50 and 100 mm). All permutations between amplitude and wavelength values are also considered. The reason at the base of the choice of such numerical parameters is twofold. Firstly, photos taken during the preparation of the specimens suggest that a perfectly planar configuration of the yarns is unlike, because the coupons are prepared without assigning a pre-stress to the yarn and that the possible wavelength l is a fraction of the coupon length (i.e. 400 mm). Such preparation of the specimens is consistent with the practical application of FRCMs on masonry walls, where pre-stress may not be induced before installation. Wavelengths investigated in the numerical exercises cover therefore a wide variability of different real configurations. Secondly, the considered amplitudes seem the most probable, not only in relation with the coupon thickness (10 mm) but also in light of direct comparison with experimental results. Starting from a trial and error best fit of the load–displacement curves, it is possible to obtain a realistic estimate of the amplitudes to consider, assuming for obvious geometric reasons the value $a = 2$ mm as an unrealistic upper bound providing results not totally in agreement with experimental evidences. An automatic mesh generation routine was used in the pre-processing phase to deal with automatically generated discretizations. The routine checks the rate of distortion of the mesh in order not to deal with unreliable meshes. Some numerical discretization used are reported in Fig. 7 for the sake of completeness, where an indication of the number of elements and nodes present in each mesh is also reported. Non linear geometrical effects are taken into account assuming a large displacements hypothesis in the FE simulations reported hereafter, even if it is expected small influence of geometrical deflection from the unstressed configuration.

2. Set 2 considers specimens with curved long edges with a longitudinal bent configuration, see Fig. 6. In particular, it is assumed that long edges are shaped following a circumference arch, with a priori assumed curvature radius. Yarns inside the specimens are in this case assumed to follow the same curvature. Such second hypothesis is consistent with the experimental observation and the photographic documentation. This initial imperfection can damage the specimen. In fact, it may occur that the installation of the bent coupons into the testing machine, as a consequence of the slenderness of the specimens, can cause cracks. Therefore this initial geometrical imperfection may result into a premature mortar crack, with a change of the overall tri-linear behavior, especially when dealing with the transition point from a phase to the following.
3. In Set 3, the coupon is assumed straight and the yarns have a pre-assigned curved configuration ($a = 1$ mm, $l = 50$ mm), but some pre-assigned transversal cracks already open before the application of the external load. Such situation was occasionally observed at the end of the preparation of some specimens and again is linked to the quite high slenderness of the coupons combined with the relatively low tensile strength of the mortar.

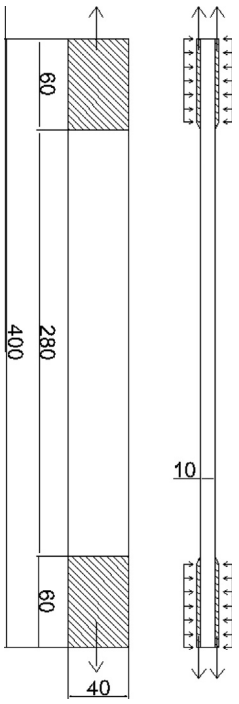

Fig. 3. FRCM specimens size (in mm).

To simulate the behavior under direct tensile test of such already damaged specimens, notches with pre-assigned depth and regularly stepped are introduced in the model. Step-length and depth of the notches are assumed in the numerical model, consistently with experimentally observed evidences. To simulate the presence of initial cracks reduced mechanical properties for the elements belonging to the notches are assumed, as shown schematically in Fig. 7.

4. Mechanical models for the constituent materials

As stated in the introduction, the objective of the present work is twofold: (1) to study and compare possible constitutive models for the cementitious matrix to simulate the experiments, (2) to examine the effects of possible initial imperfections in FRCM specimens subject to tension.

Two different FE codes [31,32] were utilized. Code [31] puts at user's disposal less sophisticated material models (namely elastic-perfectly plastic materials, eventually with limited ductility checked with user supplied subroutines), whereas in code [32] there is the possibility to deal with softening and damage in the post peak range. Whilst such latter assumption appears more realistic for mortar, it requires a much higher computational effort and experienced users. For this reason, it appears interesting to compare the performance of [31], assessing the results obtained by means of a comparison with both experimental evidences and results provided by [32]. The use of commercial codes instead of home-made models [33,34] was voluntary, with the precise final aim to enable other researchers the reproduction of results with similar models and for analogous experiments.

Three different material models were used for mortar belonging to FRCM specimens in tension, hereafter labeled as Models (A), (B) and (C). Model (A) is an elastic perfectly-plastic Mohr Coulomb material with limited ductility, Model (B) is a softening damaging material with a low fracture energy and Model (C) is the same of Model (B), but with a much higher fracture energy.

Fig. 4. Tensile test set-up.

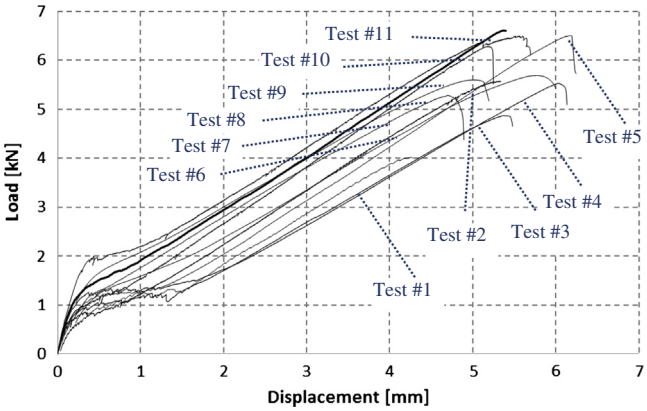

Fig. 5. Load–displacement curves, experimental results.

Mechanical properties assumed for truss elements representing yarns are depicted in Fig. 8. A typically elasto-fragile behavior was adopted, since it well approximates what happens in reality during tensile tests conducted on single yarns. The main mechanical properties (Young's modulus and ultimate tensile stress) were derived directly from the experimental tests conducted for the present study (see Section 3). These are part of a wider experimental project on FRCM composites described in [7].

As already mentioned, Model (A) was specifically conceived to represent a fast and easy tool to be used in practical design, even for parametric studies. This was possible using the FE program [31]. In this case, the softening in the constitutive curves of the cementitious matrix may not be considered rigorously, because only elastic-perfectly plastic material models are available. In order to circumvent this major limitation and to manage with softening in the framework of elastic-perfectly plastic models, an approximation of the uniaxial mortar stress–strain curve with a stepped function, as in Fig. 9, was adopted.

Since a Mohr–Coulomb failure criterion is adopted for mortar, peak tensile strength f_t is evaluated as $f_t = c/\tan\Phi$, where c is the peak cohesion and Φ is the friction angle, assumed constant during all the deformation process.

Table 2
Tensile test experimental results on the FRCM system.

	E_1 (GPa)	E_2 (GPa)	E_3 (GPa)	σ_{t1} (MPa)	σ_{t2} (MPa)	σ_u (MPa)	ε_{t1} (%)	ε_{t2} (%)	ε_u (%)	E_1^* (GPa)	σ_{t1}^* (MPa)
Average	1180.8	75.7	215.8	890.2	1099.6	3316.4	0.08	0.50	1.69	4.84	3.65
Min value	902.6	38.8	189.2	509.8	551.1	2485.1	0.04	0.24	1.27	3.70	2.09
Max value	1612.8	122.4	250.0	1119.5	164.6	4669.4	0.13	0.81	2.00	6.61	4.59
C.o.V (%)	19.6	33.1	9.20	15.2	12.6	14.0	30.9	33.7	18.2	19.6	15.2

Note:
σ_{t1}: tensile stress at point T_1.
σ_{t2}: tensile stress at point T_2.
ε_{t1}: strain at point T_1 from the extensometer.
ε_{t2}: strain at point T_2 from the extensometer.
σ_u: tensile stress at failure, point T_3.
ε_u: strain at failure, point T_3.
E_1^*, σ^*_{t1}: parameters referred to the mortar area.

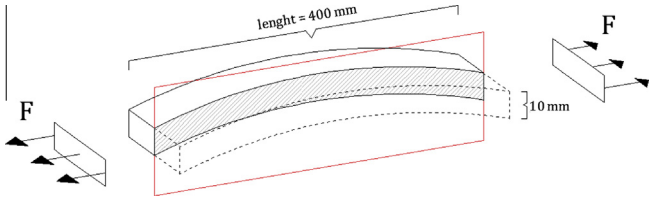

Fig. 6. Set 2 numerical exercise, geometric bent configuration.

Due to the fact that materials exhibiting softening are not available in the FE program [31], the degradation of mortar mechanical properties is modeled with a stepped function, as depicted in Fig. 9 (model A) and as already successfully done in [1] using a non-commercial FE code where the incremental problem is solved by means of sequential quadratic programming.

In order to avoid the utilization of mathematical programming and to interface directly with the commercial code [31], it was necessary to implement a user supplied subroutine to check the limited ductility of the material during the loading process (i.e. to model the softening behavior with a stepped function). Within such approximation of the actual non-linear behavior, it is in principle possible to deal with the problem of softening with the recursive solution of FE problems with elastic-perfectly plastic materials, as widely shown in [33,34], where the reader is referred to for further details. Whilst the approximation shown in Fig. 9 may appear somehow rough, however the overall behavior of the specimen is well approximated from an engineering standpoint. In any case more refined discretization can provide better approximations of the reality as extensively shown in [33], but without adding essential practical information for the problem under study.

Parameters of the stepped functions reported in Fig. 9, are obtained by least-squares best fitting on the exponential numerical curve, assumed as target data. In Fig. 9, the uniaxial behaviors of Model (B) and Model (C) are also represented (subfigure (a) refers to the tensile stress–strain curve, whereas subfigure (b) to the shear behavior).

Regarding the multi-axial behavior available in [31], an associated plasticity model is assumed for mortar obeying a classical Mohr–Coulomb strength criterion. Associativity of the flow rule appears adequate in this case considering that it is expected that the tensile region is the most active. The parameters entering into the model are f_t, the tensile Mode-I strength of the mortar and the friction angle Φ.

Assuming to keep the friction angle constant during computations, within the stepped function approximation adopted for tensile behavior, Fig. 9(a), mortar under shear is expected to behave similarly, see Fig. 9(b), with a degradation of the cohesion following an exponential low ruled by the following formula:

$$c(\kappa_2) = c_0 e^{-\frac{c_0}{G_f^{II}}\kappa_2} \tag{1}$$

being c_0 the initial cohesion and friction angle and G_f^{II} is the mode II fracture energy.

κ_2 is a scalar variable ruling the amount of softening during a pure shear deformation, which, in the framework of the classic plasticity theory is defined as $\kappa_2 = \gamma_t - \gamma_t^{el}$, being γ_t the total shear strain and γ_t^{el} the elastic part ($\gamma_t^{el} = \tau/G$).

In Model A, classic plasticity theory holds. Consequently, materials undergo the so-called associated flow rule and the total strain rate may be additively decomposed into an elastic and a plastic part. The first condition translates mathematically into the vectorial equation $\dot{\boldsymbol{\varepsilon}}^{pl} = \dot{\lambda}\nabla f$, where $\dot{\boldsymbol{\varepsilon}}^{pl}$ is the plastic strain rate vector, $\dot{\lambda}$ is the plastic multiplier rate and f is the material strength domain. The second condition is again a vectorial equation and reads as follows $\dot{\boldsymbol{\varepsilon}} = \dot{\boldsymbol{\varepsilon}}^{pl} + \dot{\boldsymbol{\varepsilon}}^{el}$, where $\dot{\boldsymbol{\varepsilon}}$ is the total strain rate and $\dot{\boldsymbol{\varepsilon}}^{el}$ is the elastic strain rate vector. In order to have an insight into the elements undergoing inelastic deformation and the amount of plasticization (and hence to univocally identify the critical elements), a scalar quantity called equivalent plastic strain is usually utilized, defined as $\varepsilon^{eq} = \int \sqrt{\dot{\boldsymbol{\varepsilon}}^{pl^T}\dot{\boldsymbol{\varepsilon}}^{pl}}$. Despite the fact that $\varepsilon^{eq} > 0$ by definition, since in the numerical applications hereafter presented only the axial stress is active, we present color patches in terms of a slightly modified version of ε^{eq}, which is kept negative when a compression axial stress acts.

The approximation with a stepped function enables, on the other hand, to carry on analyses with rigid elements and softening interfaces by means of a numerical model adapted to the study of FRCM elements recently presented in the literature [1,33,34], within a quadratic programming approach.

Models (B) and (C) where produced using the FE program [32] and adopting for mortar a Damage Plasticity Model (DPM) to accurately reproduce the main features of such material embedded into the FRCM systems. Generally, low tensile strength and softening behavior in tension are the key aspects to deal with.

DPM is essentially a concrete damage-plasticity (CDP) material already available in the standard software package, which enables to investigate the non-linear behavior of isotropic softening materials under static and dynamic loads. The model is suitable for modeling materials with distinct tensile and compressive strength, and damage parameters (see Fig. 10).

The two damage parameters used are called d_t *e* d_c, the first referred to tension and the latter to compression, Fig. 10. They can vary between 0 (undamaged state) and 1 (totally damaged state) and modify the uniaxial stress–strain behavior in the unloading

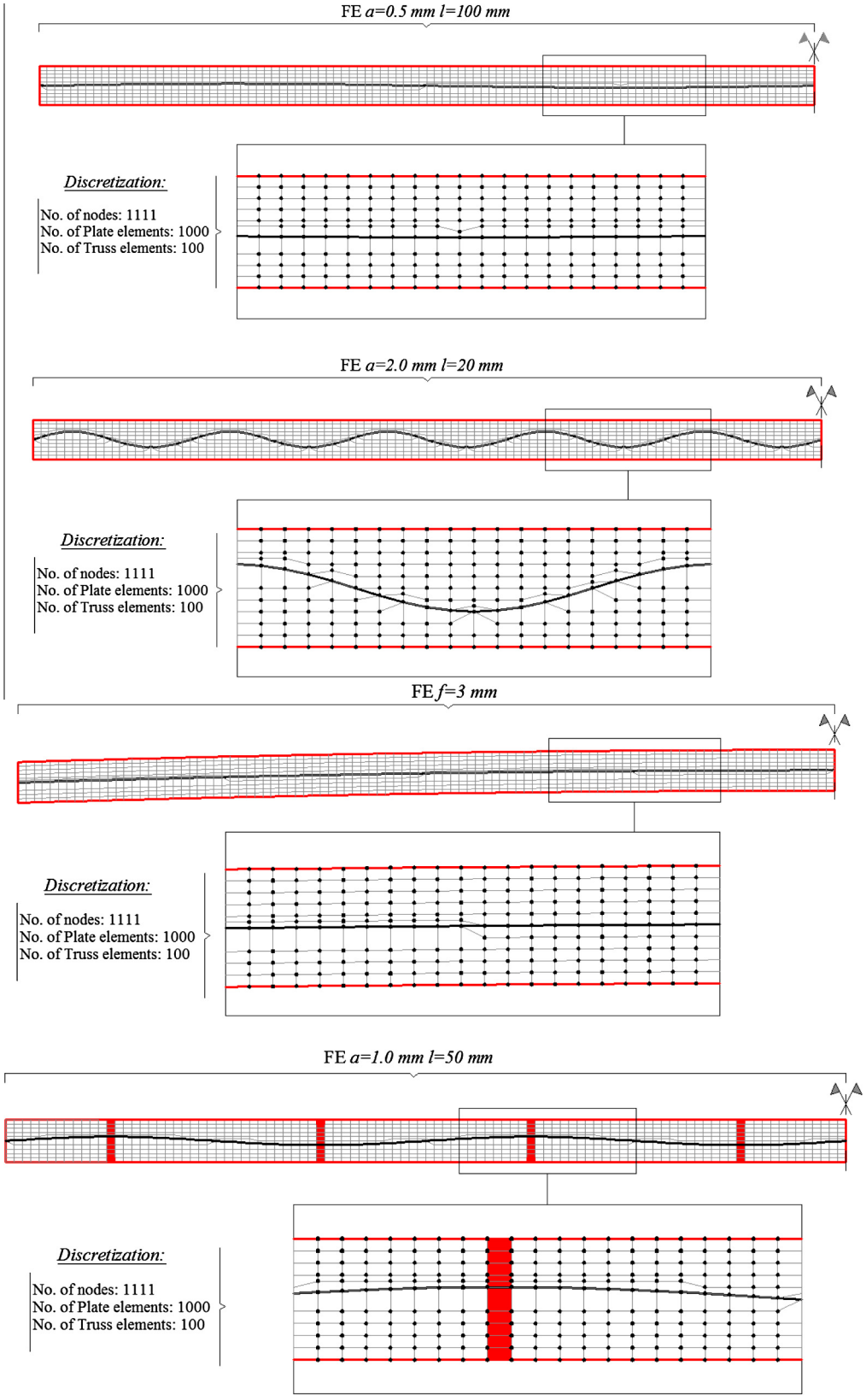

Fig. 7. Numerical FE discretization adopted to analyze FRCM subjected to tensile tests.

path, penalizing the stiffness of the descending branch by means of the well known Hooke's law as $\sigma_{t,c} = (1 - d_{t,c})E_0\left(\varepsilon_{t,c} - \varepsilon_{t,c}^{ple}\right)$ where σ_t and σ_c are the uniaxial tensile and compressive stresses, E_0 is the initial elastic modulus (undamaged state), ε_c and ε_t are the total strain in compression and tension and ε_c^{ple} (ε_t^{ple}) are the total plastic strains in compression (tension).

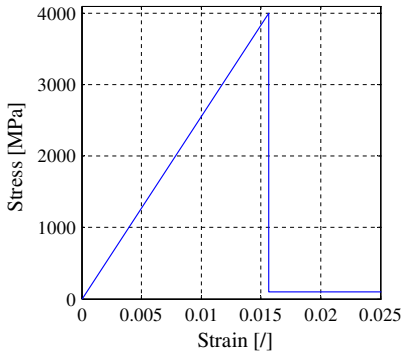

Fig. 8. Uniaxial stress–strain behavior of the yarns.

The model assumes that the two main failure mechanisms are tensile cracking and compressive crushing.

The strength domain is a Drucker Prager (DP) surface modified with an ad-hoc parameter, which distorts the limit surface in the deviatoric plane from a circle to a surface more similar to a Mohr–Coulomb one. This parameter physically represents the ratio between the distance from the hydrostatic axis of the maximum compression and tension respectively. In the simulations this coefficient was kept equal to 2/3, a value used to well approximate a Mohr–Coulomb failure criterion.

The uniaxial inelastic behavior due to the damage part is evaluated with a multi-linear softening model in both tension and compression, with strains depurated from the elastic part. The uniaxial stress strain curves for Models (B) and (C) are depicted in Fig. 9. It should be pointed out that Models (A) and (B) exhibit the same fracture energy, whereas Model (C) is similar to an elastic perfectly plastic material.

As can be noted from Fig. 9, under tensile stresses, the curve well approximates an exponential softening, which is typical of mortar and follows a mode I failure. Typically, in this case the yield function reads:

$$f_1(\boldsymbol{\sigma}, \kappa_1) = \sigma - f_t(\kappa_1) \tag{2}$$

where the yield value $f_t(\kappa_1)$ deteriorates in agreement with the following formula:

$$f_t(\kappa_1) = f_{t0} e^{-\frac{f_{t0}}{G_f^I}\kappa_1} \tag{3}$$

where f_{t0} is the initial joint tensile strength and G_f^I is the mode I fracture energy.

Similarly to κ_2, κ_1 scalar rules the amount of softening, and is defined as $\kappa_1 = \varepsilon_t - \varepsilon_t^{el}$, being ε_t the total axial strain and ε_t^{el} the elastic part of the axial strain.

While the simplified approach, Model (A) may result in a local inaccuracy in reproducing the experimental evidences (second phase in Fig. 5), drawbacks related to the utilization of the damage Models (B) and (C) stand in a less effective robustness of the FE model and in very demanding computations.

5. Numerical results

In Set 1, a family of numerical models was examined, where the yarn is supposed not-straight.

The parametric investigation was conducted using Model (A), after validation upon Models (B) and (C) for a case of technical relevance, and varying the wave length and amplitude of the imperfections as described in Section 3.

The numerical results in terms of global load–displacement curves are compared with the experimentally obtained envelope

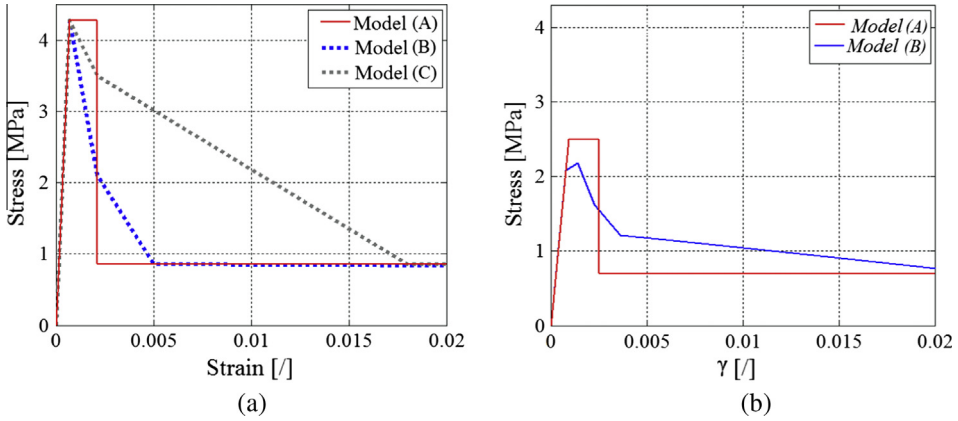

Fig. 9. Numerical uniaxial behavior assumed in the simulations for mortar. (a) Tensile behavior. (b) Shear behavior.

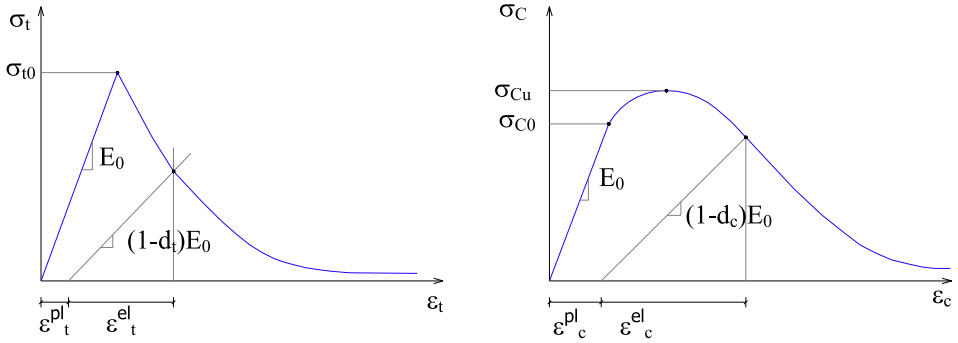

Fig. 10. Typical model for material non-linear behavior in uniaxial tension and compression.

in Fig. 11. The obtained load–displacement curves exhibit, analogously to experimental data, a behavior which may be roughly considered similar to a tri-linear curve, identified by different values of stiffness.

The first phase is characterized by the un-cracked mortar state, the second phase corresponds to the crack formation and growth, whereas the third phase is the crack-opening region. Numerical results appear in satisfactory agreement with experimental data, generally falling within the experimental upper and lower bounds.

The following remarks are worth noting:

- Phase II (second segment of the tri-linear curve) is not clearly visible in the numerical simulations using Model (A). These latter force–displacement curves, instead, exhibit a rather clear vertical drop of the load bearing capacity. Such peculiar response is clearly linked to the stress–strain relationship adopted in the tensile region ruled by a stepped strength decrease, see Model (A) in Fig. 9(a). Authors experienced that, when a multi-linear continuous damage-softening low is utilized, Model (B) in Fig. 9(a) and with a fracture energy equal to that adopted in Model (A), the two models produce similar results. When larger values of fracture energies are utilized in the damage model, Model (C), the drop of the load bearing capacity at the transition between Phase I and II is much less evident and a better approximation of the experimental behavior is achieved. A comparison among the curves obtained with Models (A), (B) and (C) for $a = 1$ mm and $l = 50$ mm is depicted in Fig. 12. As already pointed out, in absence of an experimental characterization for mortar fracture energies, two fracture energies were considered within software [32], the first exactly equal to that assumed in Model (A), the second much larger. As expected, the agreement between the results provided by the FE codes is fully consistent with the approximations introduced in Model (A) (stepped function). The satisfactory fitting obtained, at least from an engineering point of view, enables to perform simulations by means of the stepped function approximation, which is particularly indicated when a strong reduction of the computational time is needed. In fact, FE Model (C) gives a very good reproduction of Phase II real behavior, with a drop of strength that obviously tends to decrease because of the larger mortar fracture energy. This can be verified from the curves reported in Fig. 12 in the interval between 0 and 2 mm.
- The role played by the geometric parameters a and l becomes quite clear when the force–displacement curves depicted in Fig. 11 are analyzed in detail. A regular trend exhibited by the numerical curves may be observed, especially within the transition range between Phase II and Phase III. In particular, the maximum yarn curvature, expressed as $\chi_{max} = \max y''/(1+y'^2)^{\frac{3}{2}}$, appears a paramount parameter influencing the overall stiffness of the specimens, a decrease of stiffness being associated to high curvatures of the yarns. For relatively large displacements, the numerical models show a perceivable recovery of the stiffness, directly proportional to χ_{max}, clearly due to a progressive approximation of the yarns to the straight configuration. Such physically intuitive phenomenon is kept by the numerical models, where geometric non linearity is accounted for. To confirm such behavior, in Fig. 13(a) and (b), respectively, the final configuration and the transversal displacement of the yarns at the end of the simulations (failure point) are shown for $a = 0.5$ mm for four different lengths $l = 100$, 50, 20 and 10 mm. X and Y scales are maintained in all sub-figures. As can be noted, almost all specimens tend to approximate the straight configuration, compare the Y values of Fig. 13(a) and (b), with transversal maximum displacements all around 0.4 mm. Consistently, near failure, all models, whilst being characterized at the beginning by different maximum curvatures, tend to recover the stiffness of the straight yarns in tension being the mortar completely cracked. Conversely, when the mortar is still in its elastic regime, i.e. in the Phase I, all numerical models exhibit a stiffness equal to the mortar one, being the contribution of the yarn negligible.
- A detailed analysis of the stresses acting on both yarns and mortar allows having a further insight into the role player by the curvature. Some selected plots of the yarns curvature (for $a = 0.5$, 1.0, 1.5 and 2.0 mm with $l = 100$ mm) are provided in Fig. 14, whereas all the curvatures explored in the numerical campaign are provided in Table 3. According to the simulations done, it can be noted that mortar transversal sections that are called to undergo stress concentrations are located in correspondence of the maximum curvature. In Figs. 15 and 16 for the same samples (l constantly equal to 100 mm and $a = 0.5$, 1, 1.5 and 2 mm), gray-scale patches of the horizontal normal stress in the mortar elements are shown, at two different levels of external applied load, approximately corresponding to Phase I (Fig. 15) and Phase III (Fig. 16). As

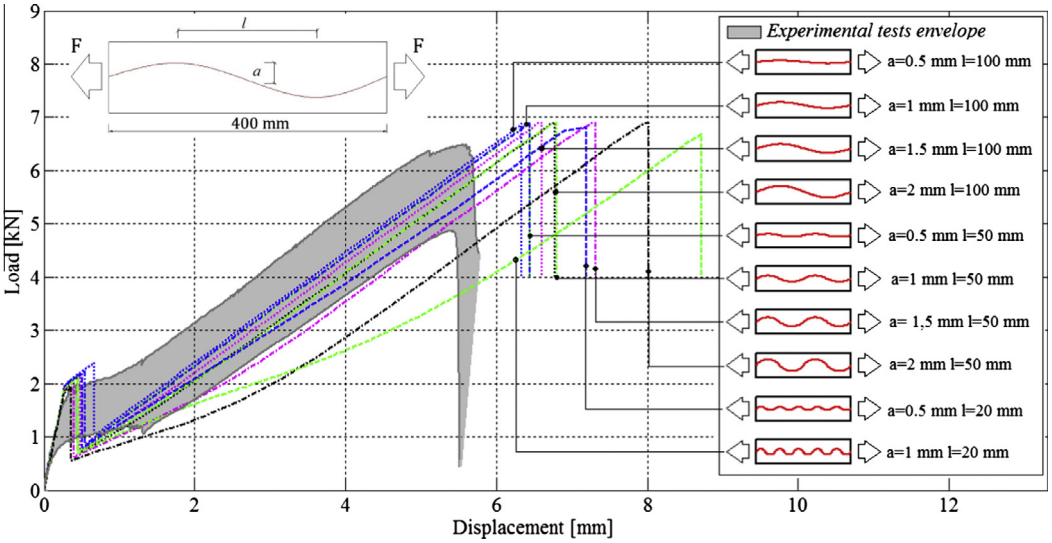

Fig. 11. Load–displacement curves: Set 1 simulations produced with Model (A).

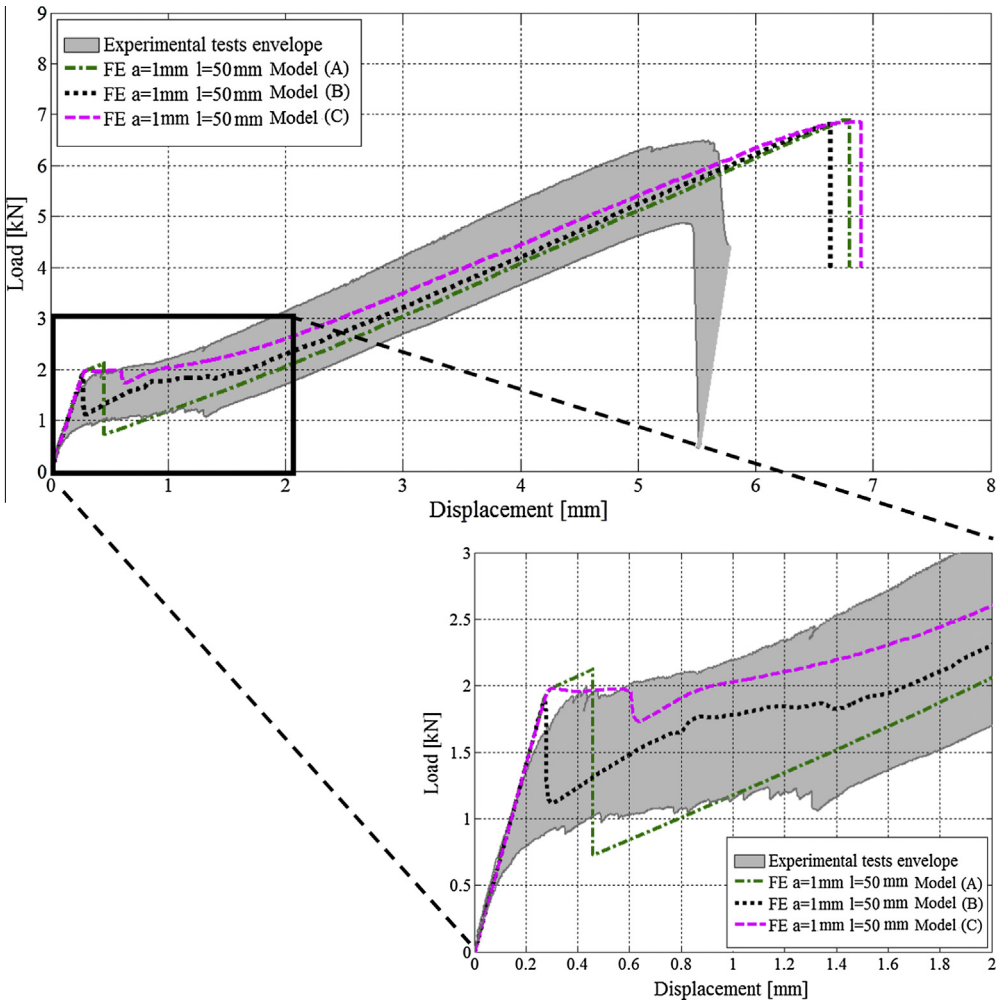

Fig. 12. Load–displacement curves obtained with Models (A), (B) and (C) (a = 1 mm, l = 50 mm).

can be noted, stress peaks are concentrated on sections where the curvature reaches the maximum absolute value. Typically, such vertical sections are those associated to the formation of transversal cracks, which in the numerical model are regularly stepped, as a consequence of the sinusoidal shape of the yarn. In Phase I, the mortar is still in the elastic phase, as demonstrated by the linear distribution of stresses along the transversal section. As expected, the peak stresses are slightly lower than the mortar ultimate strength. The slight different values of stresses exhibited by the model between the extrados and intrados are obviously a consequence of the transversal bending of the specimens, due to yarn sinusoidal shape. These effects become more evident for shorter wave lengths. Near failure, Fig. 16, an almost constant stress distribution can be found on the transversal sections, but with values sensibly lower, being the mortar almost completely cracked. When a yarn with lower wavelength is considered (l equal to 20 mm and a = 0.5, 1, 1.5 and 2 mm), the stress distribution on mortar transversal sections becomes sensibly more irregular, both at the end of Phase I (Fig. 17) and near failure-Phase III, see Fig. 18. A quite visible bending of the specimen is experienced, with mortar elements undergoing normal compression stresses at the intrados near failure. Such behavior is not surprising, because the load carrying capacity is all committed to yarns subjected to tensile stresses.

- The equivalent plastic strain provided by Model (A) at two levels of the external load, see Fig. 19 where the results for three different values of a and l are depicted, confirms again that cracks propagate on transversal sections, where the curvature reaches its maximum value, with a clear bending effect induced by the non-straightness of the yarn. Similar results are found with Model (B), as shown in Fig. 20, where the damage variable near failure is depicted (elements with a damage state greater than 0.8 are in practice almost completely cracked). A work in progress by the authors is oriented at experimentally determining the actual shape of the yarn to directly interface with the FE code without any a priori assumption, with the aim of fitting precisely the position of the cracks. Failure (end of Phase III) occurs for rupture of the yarns, i.e. according to the constitutive model assumed, when the stress in the yarn reaches its peak value, see Fig. 8. As it is possible to notice from Fig. 21, where the stress acting on yarns at three different load levels corresponding to Phase I, II and III, is depicted, excluding specimen regions near boundaries, stress exhibits again non negligible peaks in correspondence of χ_{max} and more marked stress–concentrations for small wavelengths. As expected, excluding elements near vertical edges, when mortar is totally cracked, failure occurs for rupture of the yarns in the weakened transversal sections. The numerically determined failure loads are in full agreement with the experimental results, see Fig. 11.

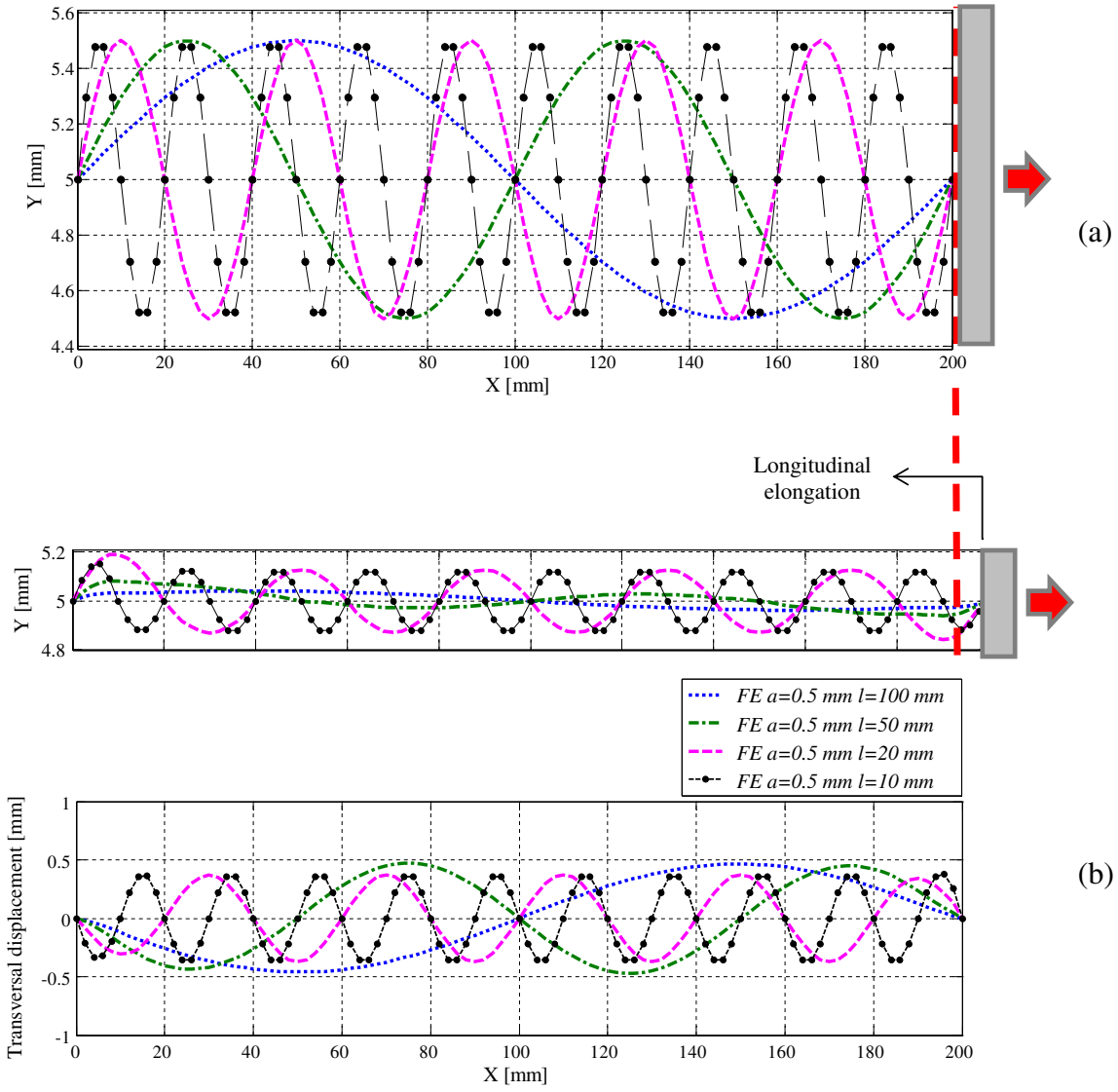

Fig. 13. (a) Undeformed and deformed shape of the yarn in the specimens at failure for $a = 0.5$ mm $l = 100$, 50, 20 and 10 mm. (b) Transversal displacement.

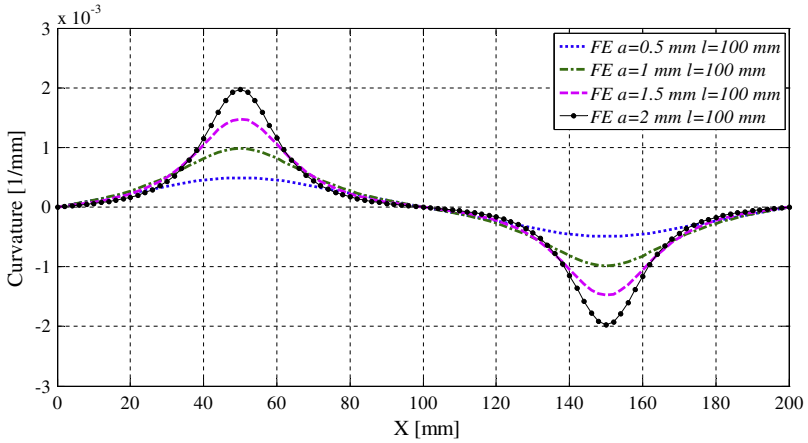

Fig. 14. Yarns curvature for $a = 0.5$, 1.0, 1.5 and 2.0 mm with $l = 100$ mm.

- In Set 1, in order to have an insight into the effects induced on numerical models by experimental data variability, with reference to the peak tensile value adopted for mortar, three different numerical simulations were repeated, the first assuming the average experimental strength. In the other two models the strength was assumed equal to the average +/− six StD.

Table 3
Maximum curvatures (1/mm) explored in the numerical simulations.

a l (mm)	20 mm	50 mm	100 mm
0.5	0.01232	0.001972	0.000493
1.0	0.02464	0.003944	0.000986
1.5	0.03697	0.005916	0.001479
2.0	0.04929	0.007888	0.001972

Looking at a detail of the global force–displacement curve near the transition between Phase I and Phase II reported in Fig. 22 for $a = 0.5$ mm and $l = 100$ mm (similar behaviors are obtained with different amplitudes and wavelengths) it can be seen that small differences occur, with an activation slightly anticipated or retarded, as expected, when the mortar presents higher or lower tensile strengths. Obviously, an uncertainty on mortar

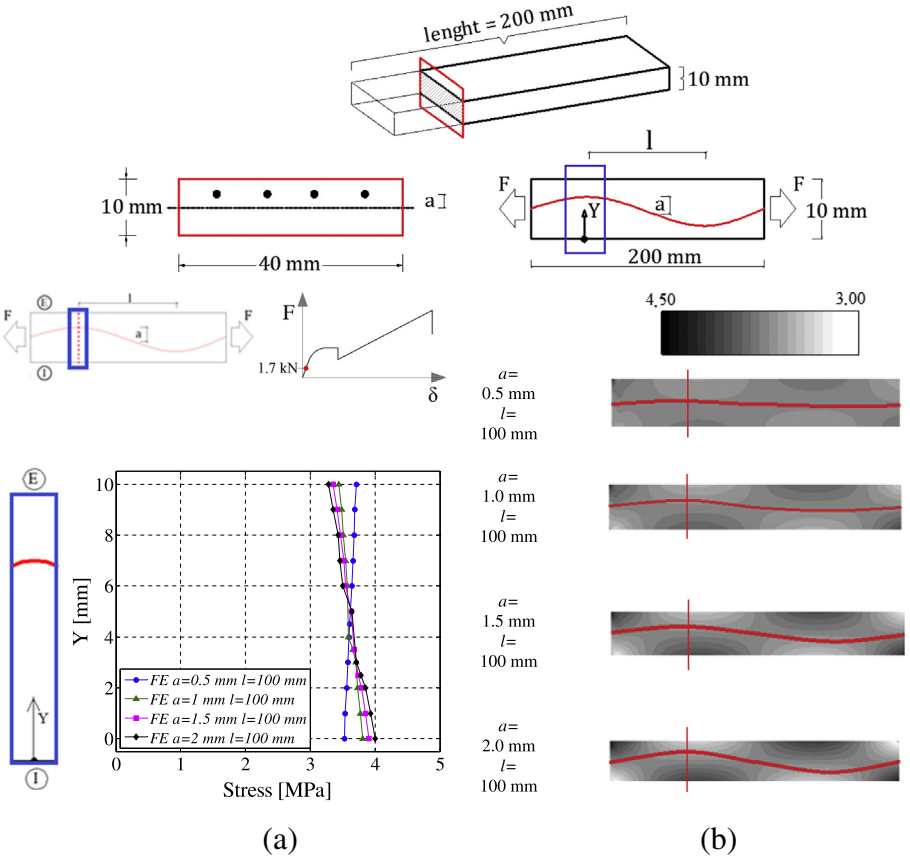

Fig. 15. (a) Stress distribution on the section E–I (curvature peak) at load = 1.7 kN (Phase I). (b) Stress patches for four different combinations of *a* and *l* parameters.

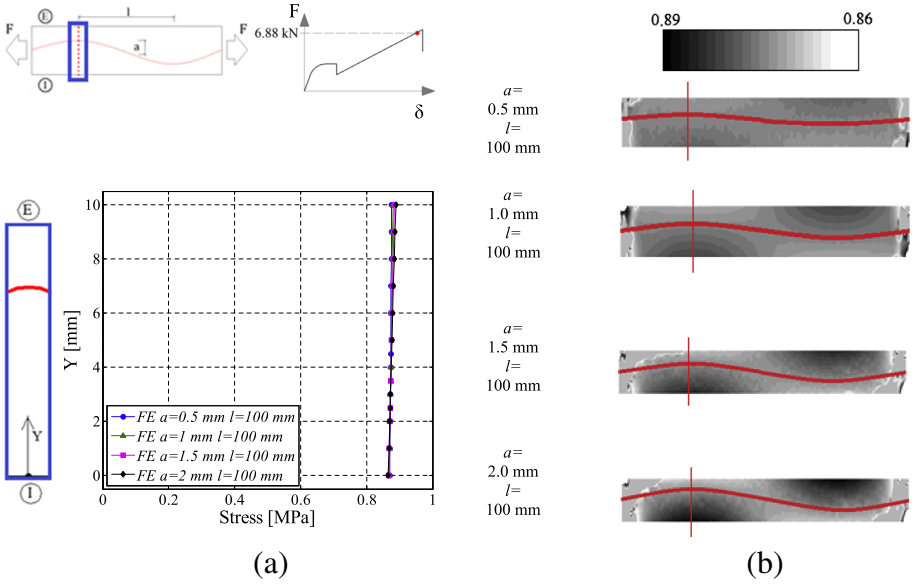

Fig. 16. (a) Stress distribution on the section E–I (curvature peak) at load = 6.88 kN (Phase III). (b) Stress patches for four different combinations of *a* and *l* parameters.

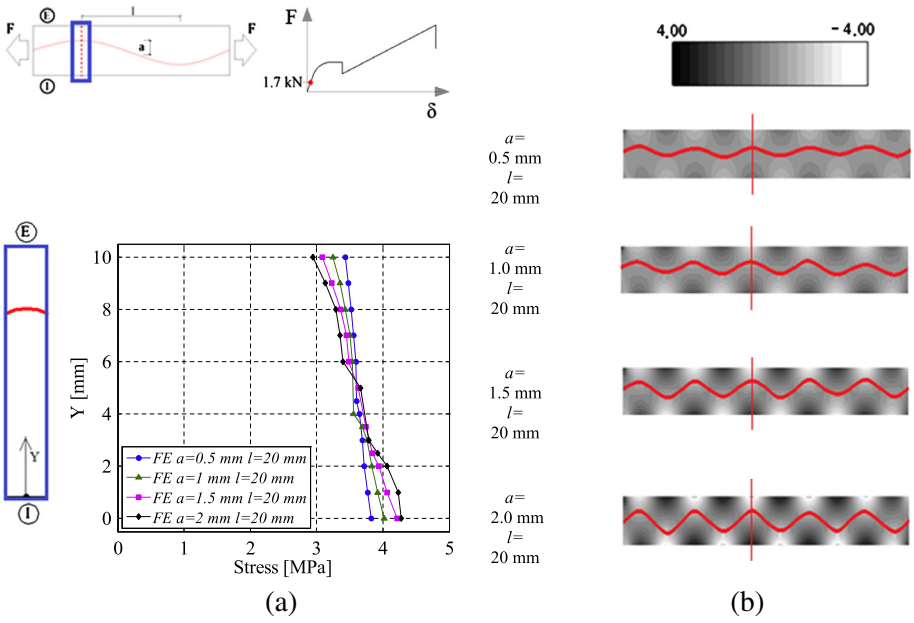

Fig. 17. (a) Stress distribution on the section E-I (curvature peak) at load = 1.7 kN (Phase I). (b) Stress patches for four different combinations of a and l parameters.

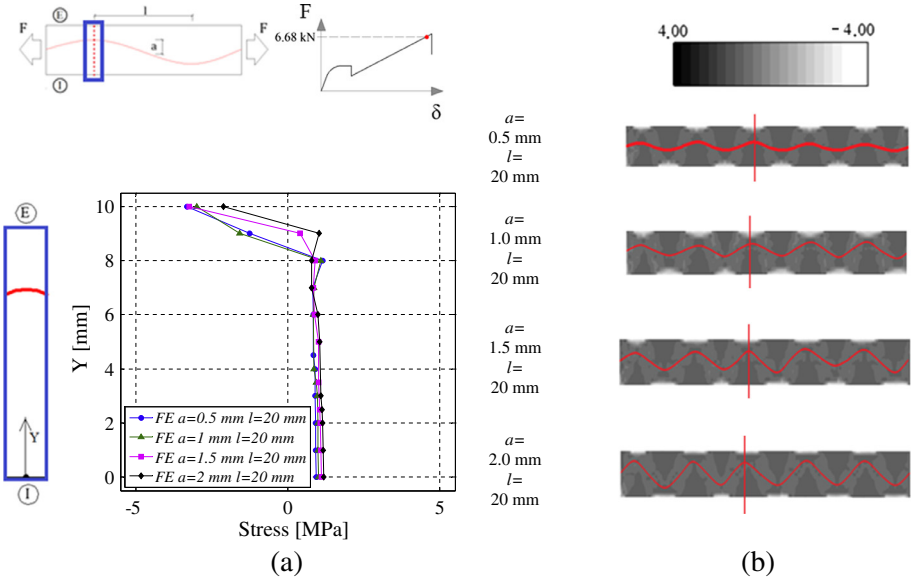

Fig. 18. (a) Stress distribution on the section E-I (curvature peak) at load = 6.68 kN (Phase III). (b) Stress patches for four different combinations of a and l parameters.

tensile strength turns out to have effect exclusively on Phase II, being mortar in Phase I purely in the elastic regime and in Phase III completely cracked.

- Let us indicate with K_1 the initial slope of the tri-linear curve in the force–displacement diagram of Fig. 5, with K_2 the slope of the intermediate region and with K_3 the final slope. From the large set of results obtained, it is particularly interesting to compare the ratios K_3/K_1 and K_2/K_1, defined as the stiffness of the curves thought as they rigorously followed a tri-linear behavior, at different wavelength and amplitude values. Results are summarized in Fig. 23, where it is possible to notice that (1) increasing the amplitude and decreasing the wavelength, the ratio K_2/K_1 visibly decreases. This was largely expected, because K_1 is essentially independent from both geometry and mechanical properties of the yarn, whereas K_2 is strongly influenced by the actual position of the yarn in correspondence of cracked sections. K_3/K_1 ratio, as expected, is always constant; this is because, within the hypothesis of geometrical non linearity adopted, the yarn tends to the straight configuration near failure, see Fig. 13, and therefore all the specimens exhibit at failure the same stiffness of the yarn when subjected to tensile stresses.
- The second set of simulations, Set 2, is done on specimens assumed already bent before their introduction into the testing machine. A geometrical imperfection is very likely, because of the reduced thickness of the specimen (10 mm) when compared with its length. Numerical simulations exhibit in this second case a behavior that is similar to that found for Set 1. In

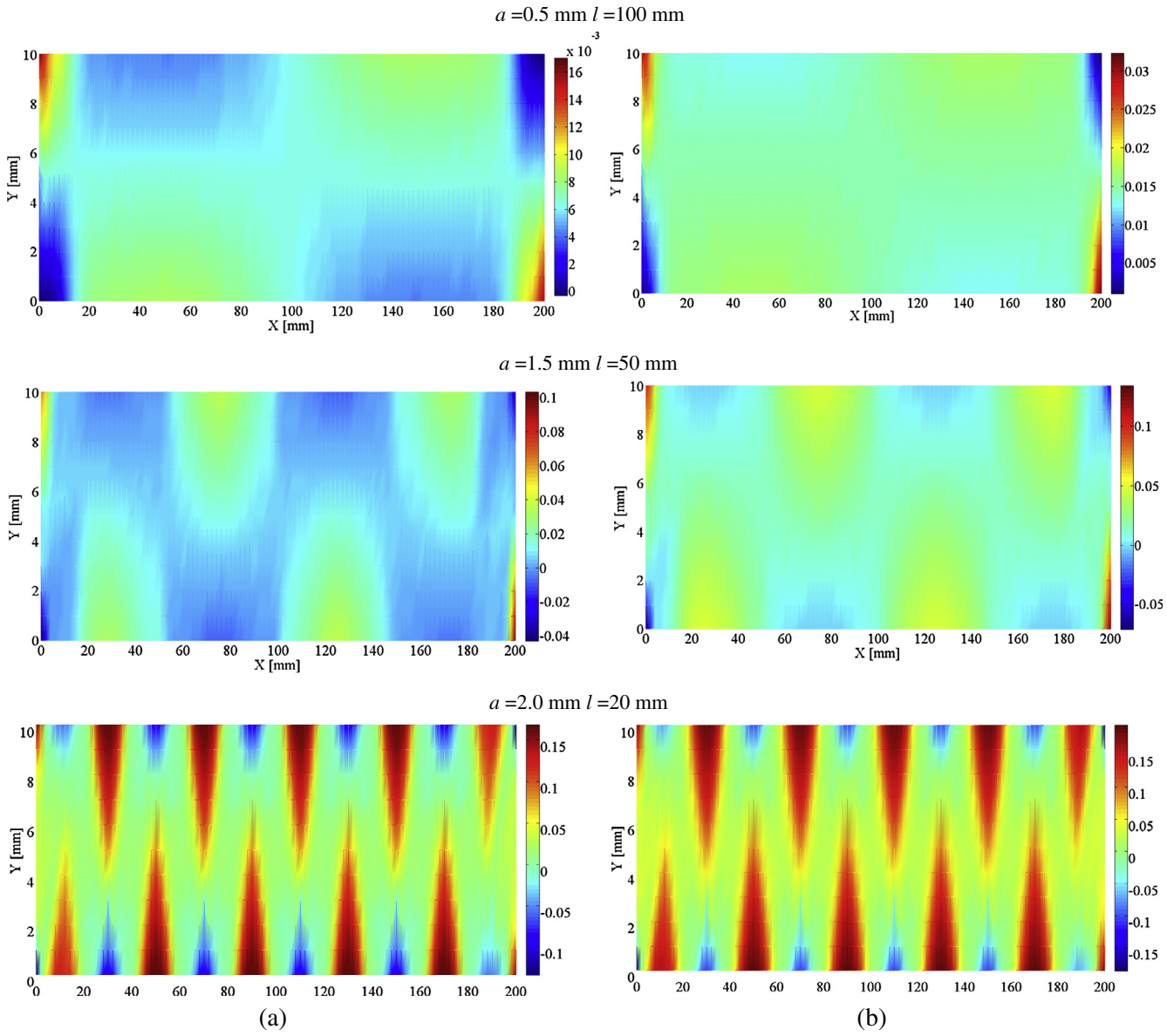

Fig. 19. Plastic strain with sign (<0 compression > 0 tension) distribution into three specimens with different values of a and l. (a) Load = 3.0 kN. (b) Load = 8.0 kN.

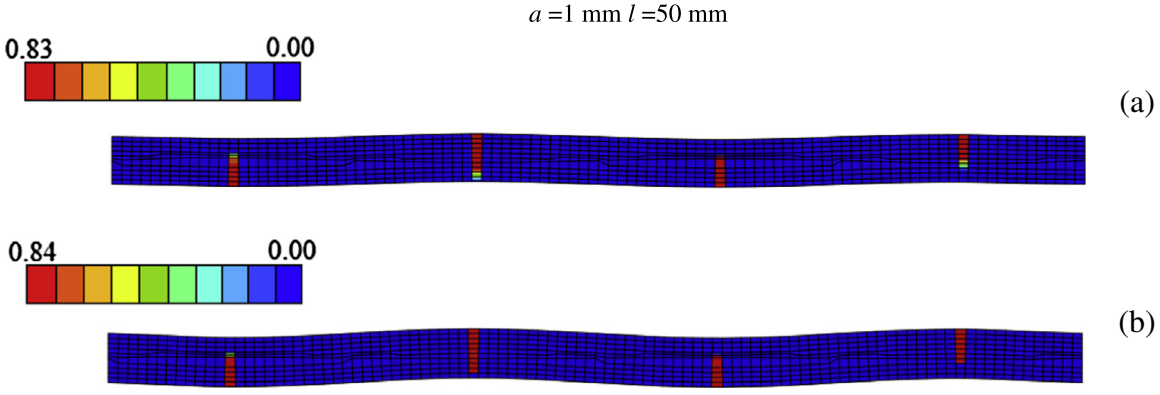

Fig. 20. Damage map obtained with Model (B). (a) Load = 3.0 kN. (b) Load = 6.8 kN.

particular, the curvature of the whole specimens plays a similar role of the curvature imposed to the yarn in straight specimens. Load displacement curves so obtained at three different curvatures of the specimens are summarized in Fig. 24 for the sake of completeness. In this case, crack occurs in correspondence of the transversal central section, as a consequence of the maximum eccentricity of the external load F. Reasonable values of eccentricity are selected, in agreement with

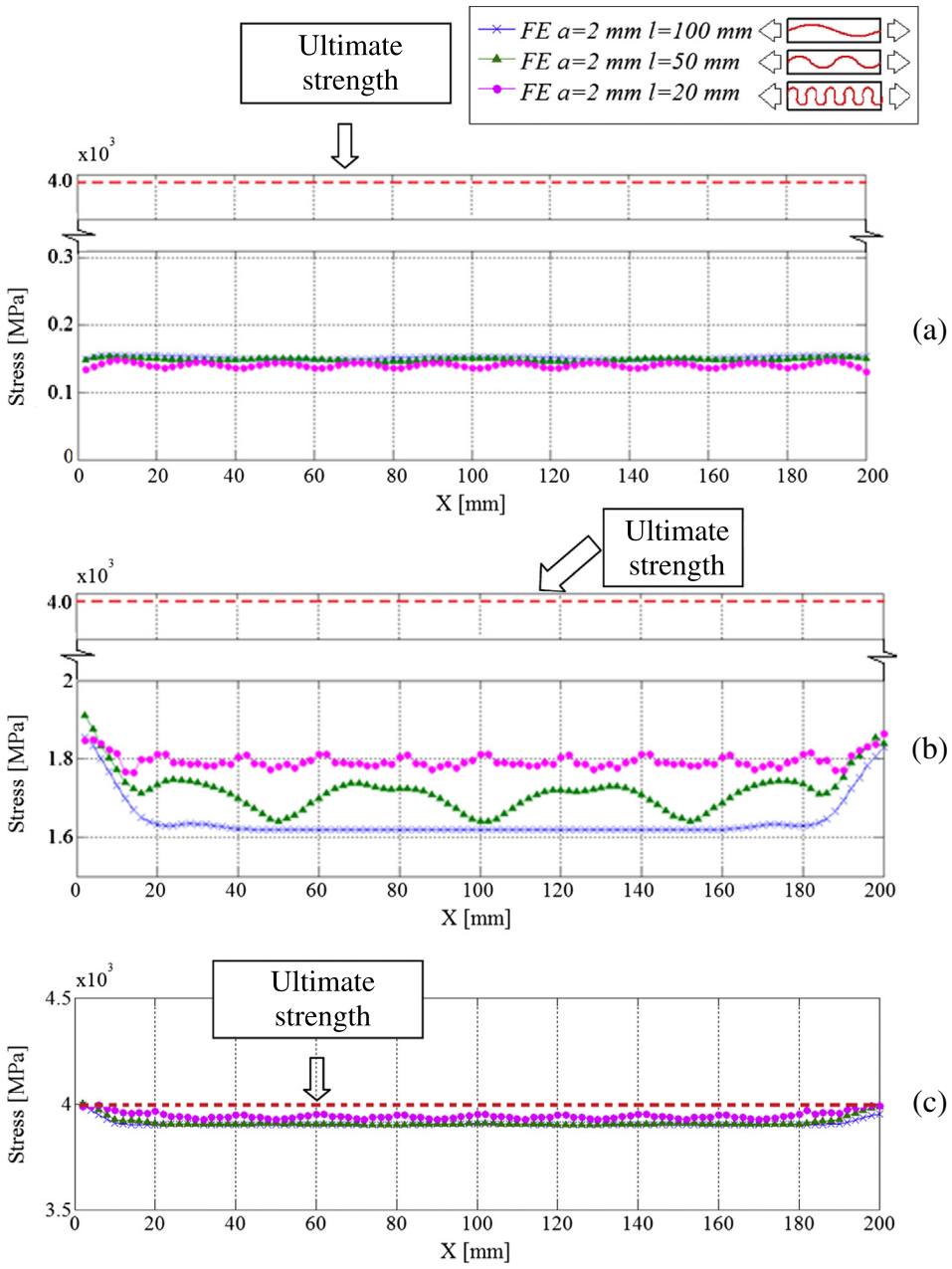

Fig. 21. Normal stress distribution on yarn for four different combinations of a and l parameters. (a) load = 1.7 kN, (b) 3.0 kN, -c: 6.75 kN.

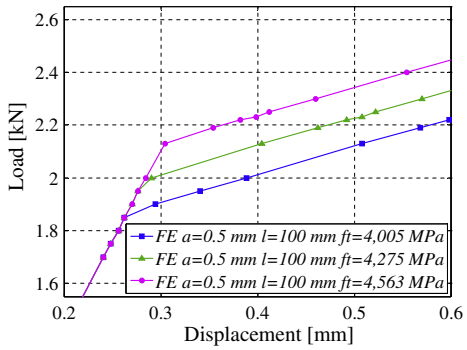

Fig. 22. Detail of the global force–displacement curve at the transition between Phase I and Phase II for different values of mortar tensile strength (a = 0.5 mm and l = 100 mm).

experimentally observed situations. While results very similar to those found for Set 1 are here experienced macroscopically, the failure mode is less in agreement with experimental evidences, showing a formation of equally stepped cracks on the specimens, different from test to test and probably linked to the imperfect pose of the yarn inside the mortar matrix, as previously discussed.

- Due to the high slenderness, specimens must be handled with extreme care, and it may occasionally occur that they microcrack before their installation on the testing machines. Microcracks are not always immediately visible but may play a crucial role in the tests, with a strong reduction of the strength in Phase II. A reasonable numerical approximation of such situation may be reproduced introducing notches to simulate the cracks, Set 3. Such numerical simulations were performed assuming very low mechanical properties for the elements in correspondence of the notches. These analyses should be

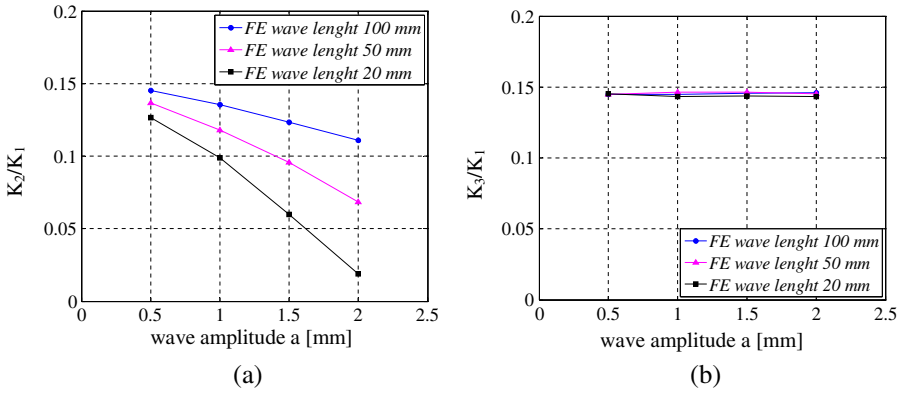

Fig. 23. K_2/K_1 ratio (a) and K_3/K_1 ratio (b) for three different wave-lengths (l = 100, 50 20 mm) and four a wave.

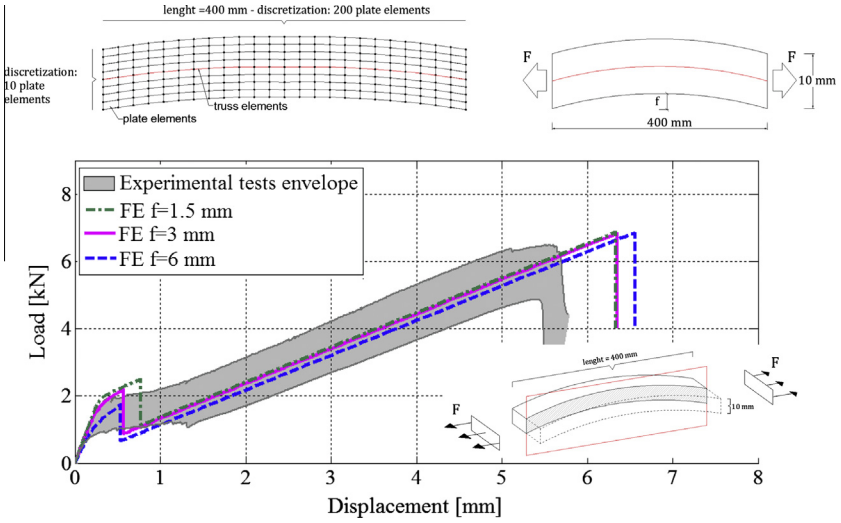

Fig. 24. Set 2 simulations. Load–displacement curves, comparison between experimental and numerical results.

repeated case by case, every time a specimen appears cracked before the test, and with a precise survey of position and depth of the cracks. A simulation with artificially generated and equally stepped notches was studied using Model (A), see Fig. 25, where the global force–displacement curves obtained by means of three different series of artificially generated notched meshes are depicted. Again and as expected, the results are similar to those obtained with Set 1. In particular the notches, because equally stepped, play the same role of the yarn wavelength. The notches depth produces effects similar to those obtained with the yarn geometric imperfections. As expected, in this case, cracks propagate on all notched transversal sections, as confirmed by the propagation of the equivalent plastic strain depicted in figures from Figs. 26–28.

6. Closing remarks

In this paper, the final results of a wide investigation on the behavior of Fabric reinforced cementitious matrix coupons under tensile tests conducted by means of 2D FE models have been presented. In order to examine the causes of the experimentally observed scatter, a simplified numerical modeling strategy has been proposed. Experimental observations gave useful hints to detect the factors that mainly influence the global behavior of the specimens tested. To separately analyze their effect, three series of simulations were performed. In all the analyses, FRCM specimens were modeled using for mortar four-noded non-linear plane-stress elements and for yarns two-noded truss elements.

In Set 1, a non-straight configuration of the yarn inside the specimens was assumed, geometrically described by a sinusoidal function, characterized by two variable parameters, the amplitude and the wavelength. In Set 2, an initial deformed configuration of the coupon due to a global bending applied before mechanical test-

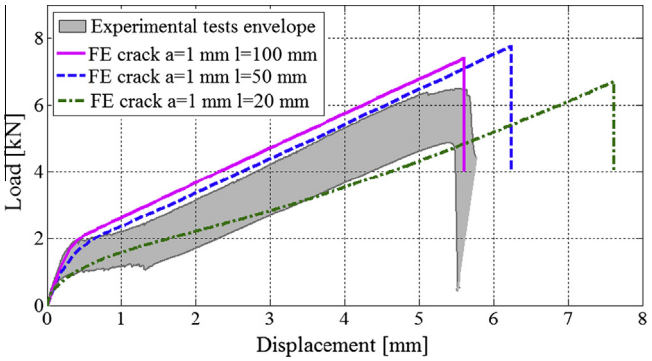

Fig. 25. Set 3 simulations. Load–displacement curves, comparison between experimental and numerical results.

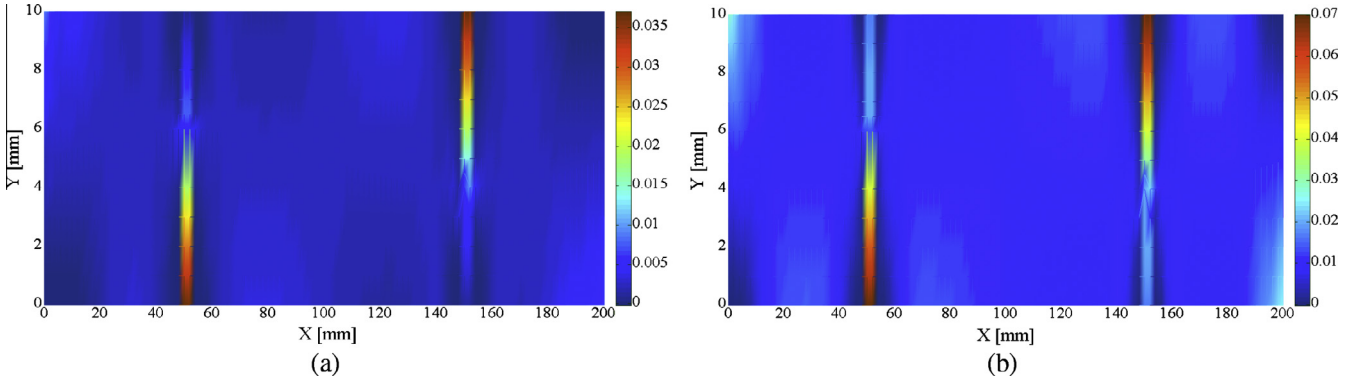

Fig. 26. Equivalent plastic strain with sign (<0 compression > 0 tension) distribution into one specimen of Set 3, a = 1 mm l = 100 mm. (a) Load = 3.0 kN. (b) Load = 6.5 kN.

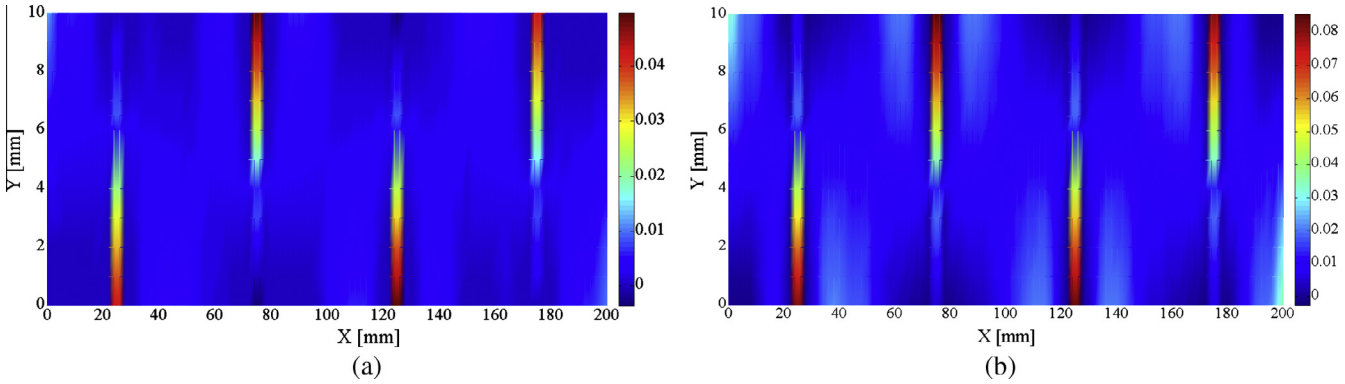

Fig. 27. Equivalent plastic strain with sign (<0 compression > 0 tension) distribution into one specimen of Set 3, a = 1 mm l = 50 mm. (a) Load = 3.0 kN. (b) Load = 6.5 kN.

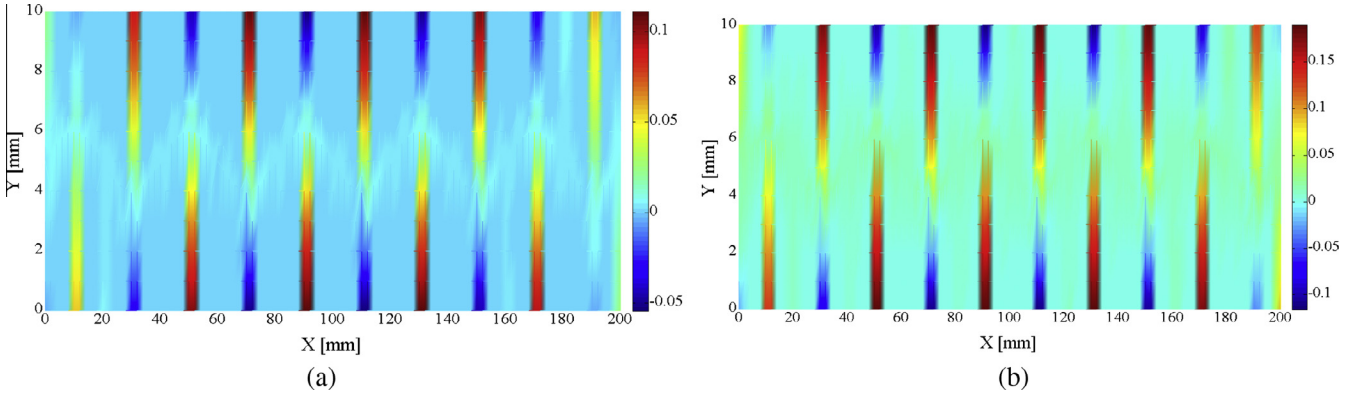

Fig. 28. Equivalent plastic strain with sign (<0 compression > 0 tension) distribution into one specimen of Set 3, a = 1 mm l = 20 mm. (a) Load = 3.0 kN. (b) Load = 6.5 kN.

ing was assumed, the specimen shape following a circumference arch. The last series of simulation, Set 3, was characterized by the assumption of an initially cracked condition of the cementitious matrix.

All the analyses gave important information on the experimental behavior of FRCM under tension and the imperfections considered separately in the three sets reasonably explain the experimentally observed scatter of the results.

The following concluding remarks are worth noting:

- The presence of a non-planar configuration of the yarns inside the coupon can influence stress and strain distributions in the specimens, with more perceivable effects at high curvatures of the yarn. Numerical simulations showed also that this latter parameter has effects on the overall stiffness of the specimens.
- As expected, another key factor influencing the global behavior of the specimens is the stress–strain relationship in tension adopted for mortar. Low fracture energy coincides with a visible drop of the load bearing capacity in Phase II, whereas higher fracture energy results in a more ductile behavior.
- Set 2 simulations demonstrated, in agreement with intuition, that an increase in the initial specimen curvature is linked to a sensible decrease of the stiffness and strength in Phase II. Increasing the external load, the coupon tends progressively to return into a straight configuration, justifying the same stiffness found near failure.
- Finally, the presence of equally stepped micro-cracks (Set 3 simulations) generally explains a reduction of stiffness at the transition between Phase II and III and, obviously, a lower load bearing capacity.

The present study was conducted with the aim of analyzing the effects that three sets of imperfections can produce on the global behavior of FRCM specimens subjected to tensile tests. It is particularly important to increase the knowledge about the behavior of such materials, also with reference to imperfections, that can be accidentally produced during the preparation phase of the coupons, but that are very common when these materials are used for retrofitting of existing structures.

Acknowledgements

These tests were performed on specimens produced using reinforcing materials and mortars distributed by Ruredil Italia. Their financial support is gratefully acknowledged. Part of the analyses were developed within the activities of Rete dei Laboratori Universitari di Ingegneria Sismica – ReLUIS for the research program funded by the Dipartimento di Protezione Civile – Progetto Esecutivo 2014.

References

[1] Carozzi G, Milani G, Poggi C. Mechanical properties and numerical modeling of fabric reinforced cementitious matrix (FRCM) systems for strengthening of masonry structures. Compos Struct 2014;107:711–25.
[2] Schwegler G. Masonry construction strengthened with composites in seismically endangered zone. In: Proc: 10th European conference on earthquake engineering; 1994. p. 2299–303.
[3] EN ISO 10618/2005. Carbon fibre – determination of tensile properties of resin-impregnated yarn; 2005.
[4] UNI EN 12390-6. Tensile hardened concrete – tensile splitting strength of test specimens; 2010.
[5] Hartig J, Jesse F, Schicktanz K, Haubler-Combe U. Influence of experimental setups on the apparent uniaxial tensile load-bearing capacity of textile reinforced concrete specimens. Mater Struct 2012;45:433–46.
[6] Arboleda, D., Loreto, G., De Luca, A., Nanni, A. Material characterization of fiber reinforced cementitious matrix (FRCM) composite laminates. In: Proceedings for 10th international symposium on ferrocement and thin reinforced cement composite, Havana; 2012.
[7] Carozzi F.G., Poggi C. Mechanical properties and debonding strength of fabric reinforced cementitious matrix (FRCM) systems for masonry strengthening. Submitted to Composite B; 2014.
[8] AC434. Proposed acceptance criteria for masonry and concrete strengthening using fiber-reinforced cementitious matrix (FRCM) composite system; 2011.
[9] Eshani MR. Strengthening of earthquake damaged masonry structures with composite materials. In: Proc: nonmetallic (FRP) reinforcement for concrete structures. Proceedings of the second international RILEM symposium FRPRCS-2; 1997. p. 681–7.
[10] Saadmantesh H. Fiber composites of new and existing structures. ACI Struct J 1991;91(3):346–54.
[11] Triantafillou TC. Composites: a new possibility for the shear strengthening of concrete, masonry and wood. Compos Sci Technol 1998;58:1285–95.
[12] Triantafillou TC. A new generation of composite materials as alternative to fiber reinforced polymers for strengthening and seismic retrofitting of structures. In: Nicolais L, Meo M, Milella E, editors. Proc: composite materials. A vision for the future. Springer-Verlag London Limited; 2011.
[13] De Caso Y, Basalo FJ, Matta F, Nanni A. Fiber reinforced cement-based composite system for concrete confinement. Constr Build Mater 2012;32:55–65.
[14] Nanni A. FRCM strengthening – a new tool in the concrete and masonry repair toolbox, concrete international. Des Construct 2012;34(4):43–9.
[15] D'Ambrisi A, Feo L, Focacci F. Experimental analysis on bond between PBO-FRCM strengthening materials and concrete. Compos Part B: Eng 2012;44(1):524–32.
[16] Hartig F, Jesse U, Haußler-Combe U. Evaluation of experimental setups for determining the tensile strength of textile reinforced concrete. In: International RILEM Conference on Material Science – MATSCI; 2010. p. 117–127.
[17] D'Ambrisi A, Focacci F, Caporale A. Strenghtening of masonry-unreinforced concrete railway bridges with PBP-FRCM materials. Compos Struct 2013;107:193–204.
[18] Ombres L. Flexural analysis of reinforced concrete beams strengthened with a cement based high strength composite material. Compos Struct 2011;94(1):143–55.
[19] Capozucca R. Experimental FRP/SRP historic masonry delamination. Compos Struct 2010;92:891–903.
[20] Prochazka P, Sejnoha M. Development of debond region of lag model. Comput Struct 1995;55(2):249–60.
[21] De Felice G, et al. Mortar-based systems for externally bonded strengthening of masonry. In press in Rilem Materials and Structures; 2014, http://dx.doi.org/10.1617/s11527-014-0360-1.
[22] Valluzzi MR et al. Round Robin test for composite-to-brick shear bond characterization. Mater Struct 2012;45(12):1761–91.
[23] Chudoba R, Graf W, Meskouris K, Zastrau B. Numerical modelling of textile reinforced concrete [Numerische modellierung von textilbewehrtem beton]. Beton-und Stahlbetonbau 2004;99(6):460–5.
[24] Peiffer F, Chudoba R. A process model for material research applied to textile reinforced concrete. In: Proc: 10th international conference on civil, structural and environmental engineering computing, Civil-Comp 2005; 2005.
[25] Chudoba R, Vořechovský M, Konrad M. Stochastic modeling of multi-filament yarns. I. Random properties within the cross-section and size effect. Int J Solids Struct 2006;43(3–4):413–34.
[26] Vořechovský M, Chudoba R. Stochastic modeling of multi-filament yarns: II. Random properties over the length and size effect. Int J Solids Struct 2006;43(3–4):435–58.
[27] Chudoba R, Jeřábek J, Peiffer F. Crack-centered enrichment for debonding in two-phase composite applied to textile reinforced concrete. Int J Multiscale Comput Eng 2009;7(4):309–28.
[28] Hartig F, Haußler-Combe U, Schicktanz K. Influence of bond properties on the tensile behaviour of textile reinforced concrete. Cement Concr Compos 2008;30(10):898–906.
[29] Zeman J, Sejnoha M. Homogenization of balanced plain weave composites with imperfect microstructure: Part I – Theoretical formulation. Int J Solids Struct 2004;41(22–23):6549–71.
[30] Vorel J, Zeman J, Sejnoha M. Homogenization of plain weave composites with imperfect microstructure: Part II – Analysis of real-world materials. Int J Multiscale Comput Eng 2013;11(5):443–62.
[31] Strand 7. Theoretical manual-theoretical background to the Strand7 finite element analysis system; 2004.
[32] ABAQUS. Theory manual, version 6.6; 2006.
[33] Milani G. Simple homogenization model for the non-linear analysis of in-plane loaded masonry walls. Comput Struct 2011;89:1586–601.
[34] Milani G, Tralli A. A simple meso-macro model based on SQP for the non-linear analysis of masonry double curvature structures. Int J Solids Struct 2012;49(5):808–34.